International Journal of Mass Spectrometry 275 (2008) 86–90

Contents lists available at ScienceDirect

International Journal of Mass Spectrometry

journal homepage: www.elsevier.com/locate/ijms

Emission of molecular fragments synthesized in hypervelocity nanoparticle impacts

C. Guillermier[a], S. Della-Negra[b], E.A. Schweikert[a,*], A. Dunlop[c], G. Rizza[c]

[a] Center for Chemical Characterization and Analysis, Texas A&M University, College Station, TX 77843-3144, USA
[b] Institut de Physique Nucléaire, UMR8608, Université Paris-Sud, 91406 Orsay Cedex, France
[c] Laboratoire des Solides Irradiés, CEA-DRECAM/Ecole Polytechnique, 91128 Palaiseau, France

ARTICLE INFO

Article history:
Received 24 March 2008
Received in revised form 19 May 2008
Accepted 19 May 2008
Available online 27 May 2008

Keywords:
Nanoparticle impact
Extreme chemistry
Secondary ions
Hydrodynamic penetration
Surface analysis

ABSTRACT

We report on experiments with Au_n nanoparticles ($100 \leq n \leq 400$) at velocities of 10–60 km/s. They are implanted virtually intact via hydrodynamic penetration. The products of the extreme pressure transient are observed by mass analyzing the ionized ejecta. Targets of labeled molecules (^{13}C-, ^{15}N-glycine) reveal fragmentation–recombination processes, producing CN^- and OCN^- with high efficiency (45%). This value is over two orders of magnitude larger than that obtained with atomic and small cluster projectiles. The experiments could simulate collisions of nanosized dust particles in interstellar space.

1. Introduction

We have reported previously on the enhanced performance of secondary ion mass spectrometry, SIMS, with massive gold projectiles such as Au_n^{q+} ($100 \leq n \leq 400$; $q = 1$–4) [1,2]. Briefly, Au_{400}^{4+} at an impact energy of $34q$ keV, produces molecular ions from low mass organics with yields of ~100% [3]. A surprising observation is the synthesis of Au-adducts, where a single Au_n^{q+} projectile is the source of energy stimulating the emission and the donor of Au atoms [4]. The new process of adduct formation is due to a different impact regime than that of overlapping collision cascades prevailing in small cluster impacts. Indeed, the projectiles considered here have distinct characteristics, they are nanoparticles and at $34q$ keV have impact velocities of tens of km/s. We show below that the projectiles are implanted virtually intact in a carbon foil, thus their interaction occurs via the mode of "hydrodynamic penetration" [5]. This process involves an extreme pressure transient at the interface of the colliding solids that lasts for a few picoseconds. The process has been mostly described in physical terms, e.g., impact light flash, melting and ejection of matter, crater formation [6]. Mass spectra of the ejecta have been obtained from impacts of energetic micron-sized projectiles [7]. There are also reports of chemical effects and reactions under varying impact conditions including those where the particle shatters in the collision with the solid [8–12]. The experiments presented here provide an approach for studying the fragmentation–recombination process associated with hydrodynamic penetration in the nanometer domain and for measuring quantitatively, the rate of molecular fragments synthesis. We have also examined the transition between this regime of the solid-particle interaction and the collision induced by atomic and small cluster ions where the constituents interact independently with the solid. To account for physicochemical reaction yields, we used glycine molecules labeled with stable isotopes (^{13}C-Gly ^{15}N-Gly) and an 1:1 mixture of these two) as targets and made the measurements at the level of single projectile impacts. In this paper we present the rates of recombination for CN^- and OCN^- made with atoms from different molecules of glycine. The rates of recombination are surprisingly high as well as the yields obtained for those recombined species.

2. Experimental procedure

The experiments were run on a set up including a liquid metal ion source (LMIS) and a Wien filter for primary ion mass selection [13]. To study the final state of implanted clusters, low doses (~10^{10} ions/cm^2) of massive gold cluster ions Au_{400}^{4+} (10 and 19 keV of energy per charge) were implanted into amorphous thin carbon foils (50 nm). These targets were examined after the

* Corresponding author. Tel.: +1 979 845 2341; fax: +1 979 845 1655.
E-mail address: schweikert@mail.chem.tamu.edu (E.A. Schweikert).

1387-3806/$ – see front matter © 2008 Elsevier B.V. All rights reserved.
doi:10.1016/j.ijms.2008.05.023

irradiation with a Transmission electron microscope (Philips CM 30), operating at 300 kV. The secondary ions resulting from the cluster-target interaction were analyzed according to their mass to charge ratio in a Time of flight mass spectrometer with a mass resolution of ~1100 at mass 75 [14]. The systematic ion emission study was carried out with massive ($100 \leq n \leq 400$, $q = 4$) and small ($1 \leq n \leq 9$, $q = 1$) gold clusters of $34q$ keV total impact energy. The secondary ion yields are the average of measurements on at least three targets. Complementary yield measurements have been performed between 19 and $34q$ keV total impact energy in order to determine the influence of the projectile velocity.

Labeled glycine powders, $^{12}C_2\ ^{15}NO_2H_5$, $^{13}C_2\ ^{14}NO_2H_5$, were purchased from Cambridge Isotope Laboratories. For the mixed targets, the powders were dissolved in distilled water and dried at ambient temperature. All targets were prepared by vapor deposition under vacuum (~10^5 Torr) on a stainless steel surface. The thickness of the sample prepared in this manner was 5 μm based on ellipsometry. The 1:1 homogeneity of the mixtures was verified with the equality of the two molecular ion peaks and the binomial distribution of the dimer ion peak measurement via TOF-MS.

3. Results and discussion

Fig. 1a reproduces a transmission electron micrograph (TEM) of a 50 nm thick amorphous carbon foil after bombardment with a low dose of 10^{10} particles/cm^2 of Au_n^{q+} with $n/q = 100$ at $10q$ keV energy. Different impacts are clearly seen in this figure. Two observations must be noted: the number of impacts visible in the micrograph corresponds to ~75% of the number of implanted projectiles; the range of diameters corresponds roughly to the size distribution of clusters of $n/q = 120$ mentioned by Bouneau et al. [13]. Two magnified impact sites are shown in Fig. 1b. Assuming spherical implants with the density of gold, the implants of 1.4 and 4 nm correspond to gold nanoparticles with 100 and 2000 atoms, respectively. Around the implanted objects the carbon foil presents a morphological difference which is assumed to be due to a stress in the solid. The width of this peripheral area is ~5 nm. The largest object presents lattice fringes. Fig. 1c shows a typical high-resolution transmission electron micrograph of the impact region of a large cluster. The same observations have been made on carbon targets bombarded with similar Au clusters of $19q$ keV total energy.

This observation of nanocrystals demonstrates that the projectile atoms penetrate in a cohesive motion. In contrast, the area surrounding the impact presents a structure modification due to the high pressure and temperature associated with the transfer of tens of keV of energy in a volume of a few thousand nm^3. It must be noted that molecular dynamics simulations of clusters (Si_n, Ar_n, Ag_n, Au_n) interacting with different solids, including graphite, show a coherent penetration in the solids with the cluster constituents remaining aggregated in the final state [15,16].

The mass spectra of the small negative secondary ions obtained under the impact of a $34q$ keV energy Au_{400}^{4+} projectile on the ^{15}N-glycine, ^{13}C-glycine and the mixed targets are shown in Fig. 2a–c, respectively. The appearance of a peak at mass 28 in the mixed glycine target mass spectra (Fig. 2c) corresponds to the $^{13}C^{15}N^-$ ion. This peak is a direct evidence of a fragmentation–recombination process occurring during the bombardment with a massive gold projectile. Likewise one observes a peak at mass 44 corresponding to the $O^{13}C^{15}N^-$ recombined ion. Peaks at masses 26 and 42 correspond to the $^{12}C^{14}N^-$ and $O^{12}C^{14}N^-$ ions, respectively, and may be due, in part, to recombination. Other fragment ions such as $CNO_2H_p^-$ ($p = 1$–3) and C_3N^- were also observed (not shown in Fig. 2). The production of the latter may result from complex fragmentation–recombination processes given that the starting target molecule of glycine contains only two carbon atoms. Also notable is the formation of complex ions involving atoms from the projectile and species from a recombination process. For instance the peak due to $Au(CN)_2$ is shown in Fig. 2d–f for the different targets studied. The peaks at masses 250 and 252 contain one recombined CN fragment. Given the constraint of a single projectile, the formation of both the recombined species and Au-adduct must occur in situ, i.e., during the impact [4].

The importance of the fragmentation–recombination process becomes apparent when computing the rate of production for the pertinent assemblies of CN^- and OCN^-. The data can be extracted with good accuracy, given that ^{15}N-glycine and ^{13}C-glycine show little signal at m/z 26, 28 and 42, 44. Thus in the case of recombined CN^-, one finds that the contributions of $^{12}C^{14}N^-$ and $^{13}C^{15}N^-$ are the same. Concurrently the yield of m/z 27 corresponding to $^{12}C^{15}N^-$ and $^{13}C^{14}N^-$ decreases by the same value. A similar observation holds for OCN^-. Recalling that the data for the "no recombination" case are from the mass spectra of ^{15}N-glycine and ^{13}C-glycine, the absolute values of the difference in yields between the mixture and the single compound samples for m/z 26, 27, and 28 are given by

$$\Delta Y_x = \left| Y_{x.M} - \left(\frac{Y_{x,N} + Y_{x,C}}{2} \right) \right|$$

where ΔY_x is the difference in yield between the mixture and the no recombination case for an ion x of $m/z = 26$, 27, or 28. $Y_{x,M}$ is the yield for the ion x from the mixture. $Y_{x,N}$ and $Y_{x,C}$ are the yields of ion x in the case of ^{15}N-glycine, ^{13}C-glycine, respectively. The total

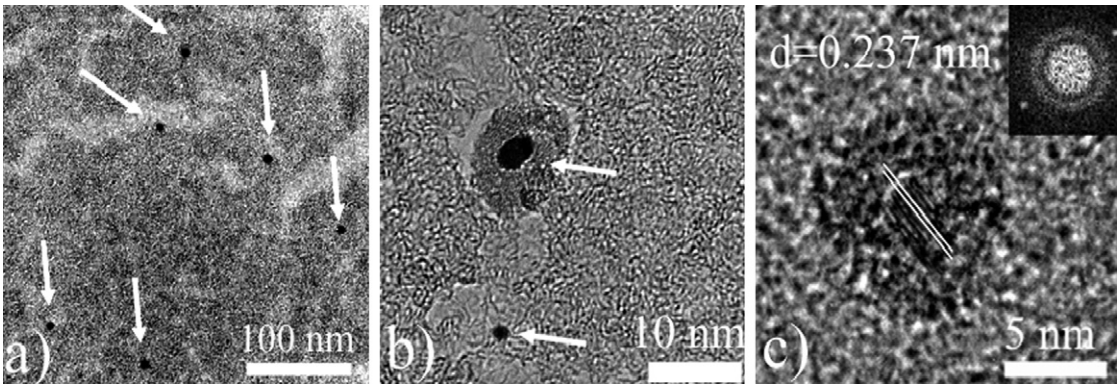

Fig. 1. TEM micrograph of a 50 nm thick amorphous carbon foil after implantation with Au_n^{q+} ($n/q = 100$) of $10q$ keV total impact energy. (a) The number of visible impacts amounts to ~75% of the number of implanted projectiles. (b) Magnified view of two impact sites. The larger object corresponds to Au_{2000}. The diameter of the stressed area surrounding the impact is 10 nm. (c) High-resolution TEM micrograph of Au_{2000} showing lattice fringes and electron diffraction pattern (insert). The 2.37 Å inter-planar distance of the nanocrystal is in agreement with the gold crystal $d(1\,1\,1)$ value.

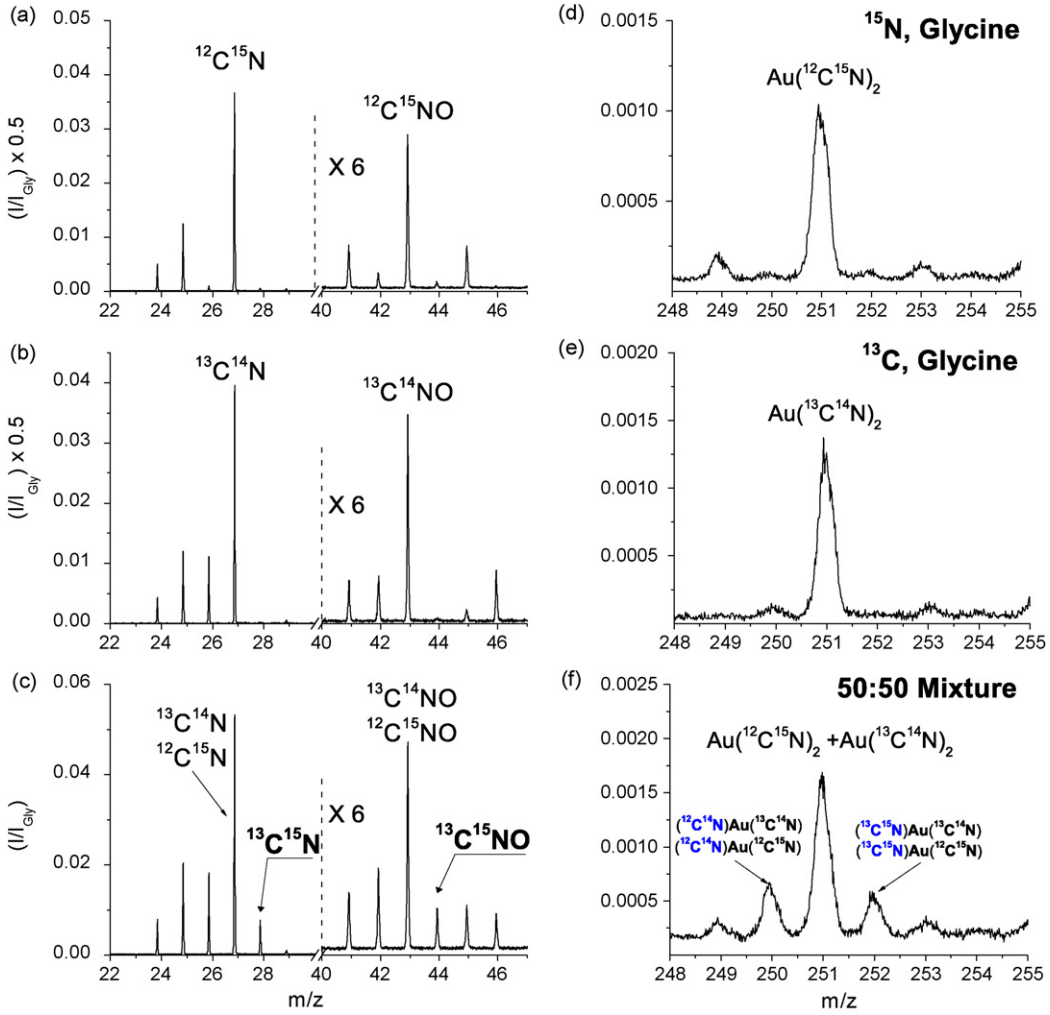

Fig. 2. Negative ion mass spectra obtained from the summation of $N_0 \sim 5 \times 10^5$ individual impacts of 136 keV Au $_{400}^{4+}$ projectiles on ^{15}N-Gly (a), ^{13}C-Gly (b), 1:1 mix of ^{15}N-Gly, and ^{13}C-Gly (c), for 22–47 mass range. The spectra are normalized to the glycine M–H$^-$ peak intensity and divided by a factor 2 in the case of the spectra (a) and (b) for ease of comparison between the two varieties of labeled glycine and their mix. (d–f) The same comparison for a range corresponding to the Au(CN)$_2$ ions for the three type of targets.

percentage of recombined CN$^-$ is the recombination rate, RR, and is defined as:

$$\mathrm{RR} = \frac{\Delta Y_{26} + \Delta Y_{27} + \Delta Y_{28}}{(Y_{27,\mathrm{N}} + Y_{27,\mathrm{C}})/2}$$

The recombination rates of CN$^-$ and OCN$^-$ are shown in Fig. 3a for a suite of Au projectiles impacting on glycine with 34q keV of total impact energy. The rates increase with the projectile size, i.e., from 7% for Au$^+$ up to ~45% for Au$_n$ projectiles with $9 \leq n \leq 400$. Similar trends and values for the recombination rate are obtained from 19 to 34q keV. The "saturation" at 45%, suggests that the hydrodynamic regime prevails for a range of impact energies and particle characteristics. For example at 34q keV, the corresponding energies range from 3.7 keV/atom for Au$_9^+$ to 340 eV/atom for Au$_{400}^{4+}$. A fraction of CN$^-$ and CNO$^-$, is emitted as gold-adducts, most prominently Au(CN)$_2^-$. The binomial distribution shown in Fig. 2f indicates that the gold atoms from individual projectile impacts react with a population of CN (produced by recombination or pre-existing) that is at equilibrium.

The production of the recombined ions requires complete fragmentation of several molecules. Key parameters in this respect are the projectile's cross-section and surface density (number of atoms/unit area). The cross-section and shape of clusters with $n < 14$ has been determined by ion mobility [17]. For massive clusters we assume a spherical shape with a cross-section, $\sigma = kn^{2/3}$. The projectile cross-sections are shown in Table 1 for the series of Au projectiles studied. The number of atoms per unit area increases from Au to Au$_9$ and is approximately equal for Au$_3$ and Au$_5$. Qualitatively, this approach explains the trends observed for the RR for the small clusters. However, for the large clusters, the number of atoms per unit area also increases with the projectile size while the RR remains mostly constant. This may indicate that the complete destruction of molecules, necessary to achieve a maximum RR, is obtained when the projectile reaches a certain surface density.

The total yield of all CN-based species, produced from both recombination and direct emission from individual molecules are shown in Fig. 3b as a function of the projectile constituent number at the same 34q keV energy per charge. The CN$^-$ and OCN$^-$ emission yields increase in an identical trend with the cluster mass. For CN$^-$, the yields obtained with the massive clusters reach 88% and therefore are 150 times larger than those for atomic gold. The enhancement reaches almost a factor 40 between the atomic ion and Au$_9$. A compilation of yields from 19 to 34q keV (data not shown here) allows a comparison at equal projectile velocities [18]. For small projectiles (Au$_{3-9}$), the enhancement can be described with a n^a ($a > 2$) relationship which is steeper than that describing

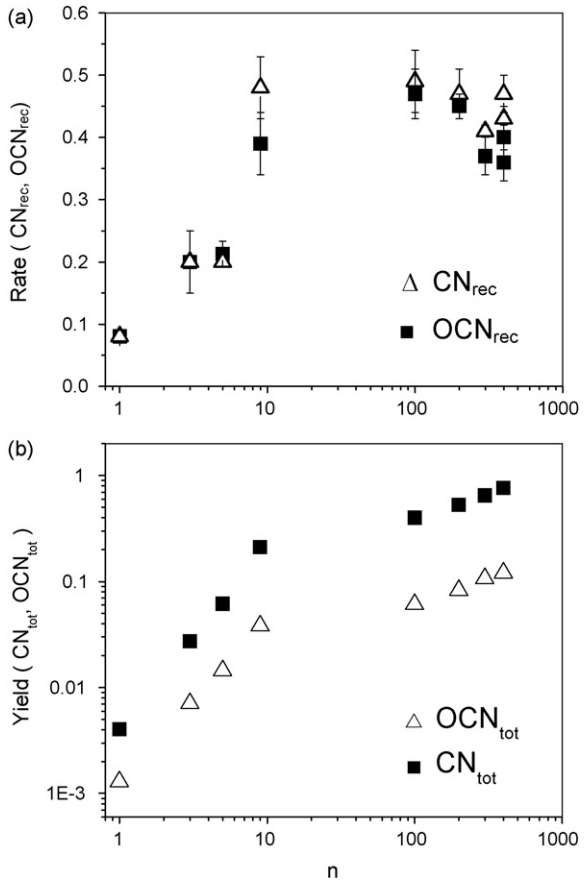

Fig. 3. Recombination rate (a) and total yields (b) for CN^- and OCN^- ions as a function of the Au_n^{q+} cluster size ($n = 1$, 3, 5, 9, $q = 1$; $n = 100$–400, $q = 4$). Results were obtained from a glycine target bombarded with projectiles of $34q$ keV total impact energy. The error bars are ≤10%.

the projectile's density and cross-section (Table 1). The non-linear enhancement observed can be explained by the overlapping collision cascades. For large clusters, the effect is smaller and in this case the trends are described by a $n^{2/3}$ relationship, i.e., corresponding to the cross-section of the clusters (Table 1) [17]. These two trends show, again, the difference between the impact of the small clusters which is related to the interaction of independent constituents, and the impact of the massive clusters for which the constituents act in a coherent way due to the compactness of the projectile.

The rates of recombination observed here can be compared with what may be obtained in the multiple collision regime with atomic ion bombardment. We monitored the emission and recombination rates of CN^- and OCN^- following implantation with a 34 keV atomic gold beam with doses of up to 6×10^{15} atoms/cm^2. The recombination rates increase with the implantation dose to reach a plateau at 6×10^{14} atoms/cm^2 (0.06 atoms/Å^2) with an average value of ~58%. This maximum value is obtained when 85% of the target is destroyed. The difference between the recombination rate of ~45% obtained in nanoparticle bombardment and that of ~58% after Au implantation can be explained by the modification of the chemical composition of the target due to its destruction in the latter case.

An implantation of 0.06 atoms/Å^2 is required for complete destruction of the area exposed to bombardment and hence for achieving a maximum recombination rate. For Au_9 and massive clusters the cross-sections and the atomic densities per unit area (Table 1) lead to more than 0.06 atoms/Å^2. For small clusters Au_{3-5} the straggling of the individual gold atoms in the solid increases the projectile cross-section which decreases the efficiency of target destruction. The efficiency of small clusters to cause fragmentation and thus their rate of recombination depends on the density of the elastic collisions in the track of the projectile. In the case of the massive clusters which remain intact during their penetration in the solid, the fragmentation–recombination is not caused by individual atomic collisions but arises from the compression and heating of matter at the interface of the colliding solids.

Table 1
Listing of the cluster projectiles used in this study at $34q$ keV total energy

Ion	Energy/atom (keV/Au)	Velocity (km/s)	Cross-Section (Å^2)	Number of atoms (Å^2)
Au	34	180	31	0.028
Au_3	11.3	110	41	0.075
Au_5	6	78	57	0.08
Au_9	3.7	61	76	0.12
Au_{100}	1.36	37	337	0.29
Au_{200}	0.68	26	534	0.37
Au_{300}	0.45	21	700	0.42
Au_{400}	0.34	18	849	0.47

4. Conclusions

The impact of a nanoparticle in a low Z solid involves a proportionately large displacement of matter as shown by MD simulations and inferred from TEM images. The case of hydrodynamic penetration studied here creates conditions for picosecond chemistry under extreme conditions of pressure and temperature and by virtue of shallow penetration, under conditions where products are readily observed. The difference between the atomic ions and the clusters and, even more, the massive clusters, resides in the simultaneity of the reactions observed during one single impact. The comparison between the recombination and emission rates shows the transition region from conditions where the cluster constituents interact independently (with or without overlapping of their collision cascades) to those where a hot spike due to hydrodynamic effects dominates. The nanoparticle impacts lead to emissions from two distinct processes. One involves "extreme ion chemistry", i.e., atomization with high rates of recombination and results in thermodynamically stable fragments such as CN^- and OCN^-. Simultaneously, there is an efficient emission of molecules ionized in the gas phase by electron attachment, an advantageous feature of nanoparticle bombardment for chemical analysis [1–3,14]. The experiments presented here allow to study the dynamics of matter under conditions such as those exemplified with the impact of hypervelocity nanosized dust particles on solids in interstellar space [19]. More generally, they may serve as a microscopic analog for assessing reactive processes in macroscopic impacts [20].

Acknowledgements

We thank M. Pautrat for fruitful discussions. E.A.S. thanks the R.A. Welch Foundation (A-1482) and NSF (CHE-0449312) for support. S.D.N. thanks the CNRS "direction des relations européennes et internationales" for funding a collaborative project.

References

[1] A. Novikov, M. Caroff, S. Della Negra, M. Fallavier, Y. Le Beyec, M. Pautrat, J.A. Schultz, A. Tempez, A.S. Woods, Rapid Commun. Mass Spectrom. 19 (2005) 1851.
[2] Z. Li, S.V. Verkhoturov, E.A. Schweikert, Anal. Chem. 78 (2006) 7410.
[3] C. Guillermier, S. Della Negra, R.D. Rickman, V. Pinnick, E.A. Schweikert, Appl. Surf. Sci. 252 (2006) 6529.

[4] C. Guillermier, S. Della Negra, R.D. Rickman, G.J. Hager, E.A. Schweikert, Int. J. Mass Spectrom. 263 (2007) 298.
[5] H. Fechtig, E. Grun, J. Kissel, Lecture Notes in Physics, vol. 48, Springer-Verlag, 1976, p. 607.
[6] S. Kempf, R. Srama, M. Horanyi, M. Burton, S. Helfert, G. Moragas-Klostermeyer, M. Roy, E. Grün, Nature 433 (2005) 289.
[7] D.E. Austin, R.L. Grimm, H.L.K. Manning, C.L. Bailey, J.E. Farnsworth, T.J. Ahrens, J.L. Beauchamp, J. Geophys. Res. 108 (2003) 5038.
[8] J. Kissel, F.R. Krueger, Nature 326 (1987) 755.
[9] G.G. Managadze, W.B. Brinkerhoff, A.E. Chumikov, Geophys. Res. Lett. 30 (2003) 1247.
[10] I. Schek, T. Raz, R.D. Levine, J. Jortner, J. Chem. Phys. 101 (1994) 8596.
[11] R.G. Cooks, T. Ast, M.A. Mabud, Int. J. Mass Spectrom. 100 (1990) 209.
[12] M.J. Van Stipdonk, V. Santiago, E.A. Schweikert, J. Mass Spectrom. 34 (1999) 554.
[13] S. Bouneau, S. Della Negra, J. Depauw, D. Jacquet, Y. Le Beyec, J.P. Mouffron, A. Novikov, M. Pautrat, Nucl. Instrum. Methods B 225 (2004) 579.
[14] R.D. Rickman, S.V. Verkhoturov, G.J. Hager, E.A. Schweikert, Int. J. Mass Spectrom. 241 (2005) 57.
[15] S.J. Carroll, P.D. Nellist, R.E. Palmer, S. Hobday, R. Smith, Phys. Rev. Lett. 84 (2000) 2654.
[16] C. Anders, H.M. Urbassek, Nucl. Instrum. Methods B 228 (2005) 57.
[17] S. Gilb, P. Weis, F. Furche, R. Ahlrichs, M.M. Kappes, J. Chem. Phys. 116 (2002) 4094.
[18] C. Guillermier, S. Della Negra, M. Pautrat, J. Depauw, E.A. Schweikert, in preparation.
[19] T.J. Millar, D.A. Williams (Eds.), Dust and Chemistry in Astronomy, IOP, Bristol, 1993.
[20] J. Jortner, Phil. Trans. R. Soc. B 361 (2006) 1877.